Master's thesis

NTNU
Norwegian University of Science and Technology
Faculty of Engineering
Department of Energy and Process Engineering

Filip Grevle Lolland

Optimization of a MAV helicopter for realistic flight conditions

Master's thesis in Mechanical Engineering
Supervisor: R. Jason Hearst
Co-supervisor: Eleonora Piersanti

March 2021

NTNU
Norwegian University of
Science and Technology

Filip Grevle Lolland

Optimization of a MAV helicopter for realistic flight conditions

Master’s thesis in Mechanical Engineering
Supervisor: R. Jason Hearst
Co-supervisor: Eleonora Piersanti
March 2021

Norwegian University of Science and Technology
Faculty of Engineering
Department of Energy and Process Engineering

NTNU
Norwegian University of
Science and Technology

Problem description

A small UAV helicopter will be designed using computational fluid dynamics (CFD) tools and a physical model will be tested at realistic Reynolds numbers in a wind tunnel. The thesis will include a literature review on the aerodynamics of bluff bodies and helicopters, the impact of turbulence on bluff body aerodynamics, various CFD optimization strategies, and experimental methods for turbulence generation and force measurements. This will lead into a CFD study where the body of the helicopter (without rotors) is optimized to reduce drag given certain physical design constraints. This will be followed by an experimental campaign to confirm the CFD optimization results and shed greater light on the flow physics. Two to three models will be 3D printed and forces will be measured on the body in the wind tunnel. Reasonable experimental preparation will be required, including preparing the physical models, preparing a sting to hold the models, choosing a relevant load cell to perform the measurements, and measuring the turbulence conditions. The incoming flow conditions to the helicopter model will be varied by changing the angle-of-attack, the Reynolds number, and the incoming turbulence conditions. The intention is that the final thesis is written in paper-format.

Remark on experimental incoming turbulence conditions

The active grid at the large closed loop wind tunnel at NTNU was not finished in time to be used in this thesis. The varying turbulence conditions are therefore excluded from the thesis, however a literature review of the impact of different turbulence conditions is given.

Summary

In this master thesis drag on Micro Aerial Vehicle (MAV) helicopters has been investigated using the open-source CFD code OpenFOAM® and experiments in the large wind tunnel at NTNU. The purpose has been to develop a simple CFD-based optimization routine to reduce the drag on MAVs. CFD-simulations and optimization is performed using a steady solver with the RANS-equations and the Spalart-Allmaras turbulence model. The CFD-optimization is followed by an experimental campaign where five of the models developed in the optimization routine have been 3D-printed and tested experimentally. Both simulations and experiments are performed without a rotor on the MAV helicopter. The experimental results are used to validate the CFD-study and shed a greater light on the flow physics, as more angles of attacks are tested. It is shown in the experiments that the drag is Reynolds number independent in our tested range, from $Re = 16000$ to $Re = 41000$, where the width of MAV model is used as the length scale. The manual optimization method succeeds to find a model with improved performance compared to the origin. Validation of the CFD-results is done by comparing drag coefficients from the experiment with CFD. The experiments and CFD shows good agreement in the drag coefficient for high angles of attack, $\alpha = 45\,\text{deg}$, however at $\alpha = 0\,\text{deg}$ the deviation between CFD and experiment is as much as 50%. A part of this thesis has also been to contribute to the refurbishment of the test-section in the large closed loop wind tunnel at NTNU, this is shown in Appendix B.

Sammendrag

I denne masteroppgaven blir luftmotstand på små luftfarkost (MAV) helikoptre undersøkt ved bruk av numeriske strømningsberegniger(CFD) med den åpne kildekoden OpenFOAM® og med eksperimenter i den store vindtunnelen til NTNU. Målet har vært å utvikle en enkel CFD-basert optimeringsmetode for å redusere luftmotstand på MAVs. CFD-simuleringer og optimering blir utført med en stasjonær løsningsmetode hvor RANS-ligningene løses med Spalart-Allmaras turbulensmodell. Etter CFD-optimeringen utføres det eksperimenter på fem forskjellige MAV-modeller som har blitt designet i optimering og deretter 3D-printet. Simuleringer og eksperimenter gjøres uten en rotor på helikopteret. Eksperimentelle resultater brukes til å validere CFD-modellen og gi en bedre forståelse av strømningen. Det vises at luftmotstanden er uavhenig av Reynoldstallet i Reynoldsregimet vi tester, fra $Re = 16000$ til $Re = 41000$, hvor bredden til MAV-helikopteret er brukt som lengdeskala. Optimeringsmetoden finner flere modeller som er bedre enn utgangspunktet og gir lovende resultater. Validering av CFD-resultateten er gjort kun gjennom luftmotstandskoeffisienter. CFD og eksperimentelldata stemmer godt overens for høye angrepsvinkler, $\alpha = 45\,\text{deg}$, men ved lavere angrepsvinkler, $\alpha = 0\,\text{deg}$, er det tidvis store forskjeller mellom eksperiment og CFD. En del av denne masteroppgaven har også vært å bidra til oppussingen av NTNU sin store vindtunnel, hvor også eksperimentene har blitt utført. Dokumentasjon på arbeid utført på vindtunnelen finnes i Appendiks B.

Acknowledgement

I would like to thank you my supervisor Dr. R. Jason Hearst for supervising my thesis and taking me onboard. Magnus Kyrkjebø Vinnes for experimental advice, guidance and leading the construction activity of the new wind tunnel test-section. Leon Li for data from the homogeneity scan of the wind tunnel test-section and hot wire measurements. FLIR Unmanned Aerial Systems for lending me the ATI load cell and my supervisor at FLIR Unmanned Aerial Systems, Eleonora Piersanti, for all the help from start to finish with CFD, literature review, thesis structure and general guidance. Finally I would like to thank you the experimental fluids group at NTNU for all insightful meetings and discussions, as well as everyone involved in the refurbishment of the test section of the large closed loop wind tunnel at NTNU.

Preface

The thesis is presented in an article format with the American Institute of Aeronautics and Astronautics (AIAA) Journal article style as template. The style guide provided by AIAA has been used.

The main document is followed by appendices detailing construction activities to prepare the new wind tunnel test-section for experiments and a background for the numerical simulations.

Contents

I Introduction and aims **1**

II Numerical methods **2**

III Experimental Techniques **5**
III.A Experimental Set-up 6
III.B Force Measurements 6

IV Results and Discussion **8**
IV.A CFD based optimization 8
IV.B Experimental results 12
IV.C Validation of the numerical model 12

V Conclusions **14**

Appendix A Numerical simulations **17**
A.A Turbulence model 17
A.B Grid Convergence method 17

Appendix B Wind tunnel refurbishment **19**

List of Figures

1 Numerical domain used in OpenFOAM® for all simulations. 3
2 Plot of residuals and a monitored variable, C_D, indicating iterative convergence. 4
3 Visualization of the mesh used for CFD-simulations. 5
4 Homogeneity scan of the test cross-section used in the wind tunnel. 6
5 Schematic of the experimental set-up. 7
6 The model "Basic". 8
7 The models developed in the optimization procedure. 10
8 Velocity field around five models computed with OpenFOAM®. 11
9 Drag coefficient plotted versus angle of attack for three models. 12
10 Angle of attack plotted versus drag coefficient for all models. 13
B.1 Frame mounting for the wind tunnel test section. 19
B.2 Sanding and painting of steel plates. 19
B.3 Dismantling of the old wind tunnel test section 20
B.4 Building a structure around the load balance. 20
B.5 Overview of the wind tunnel. 21

List of Tables

1 Boundary conditions used for all simulations in OpenFOAM®. 3
2 Grid convergence study performed using the GCI-method. 4
3 Results from the CFD optimization with the best models marked in **bold**. 9
4 Comparison between experimental values and computational drag coefficients at $\alpha = 0\,\text{deg}$. 13
5 Comparison between experimental values and computational drag coefficients at $\alpha = 45\,\text{deg}$ 13
6 Comparison between the Figure of Merits computed from CFD and Experiments. 14
A-1 Default coefficients used in the Spalart-Allmaras turbulence model in OpenFOAM®. 17

Optimization of a MAV for realistic flight conditions

Filip G. Lolland *
Norwegian University of Science and Technology, Kolbjørn Hejes vei 1D, 7034 Trondheim, Norway

Micro Aerial Vehicles (MAVs) operate in a low Reynolds number regime, $1 \times 10^3 < Re < 1 \times 10^5$**, in the atmospheric boundary layer. High drag as a consequence of the low Reynolds numbers limits the flight time of MAVs. Low flight speeds** $(< 20\,\mathrm{m/s})$ **limit the operational window, making MAVs unable to fly in strong winds and gusts. In this work we investigate the drag coefficient on different MAV helicopter bodies to increase the flight time of MAVs and the corresponding operational window. A simple numerical optimization method to reduce the drag using computational fluid dynamics (CFD) is suggested and experiments are performed to validate the results. The experiments measured the drag on five different helicopter body designs, chosen from a CFD optimization study. It is shown that the drag coefficient is Reynolds number independent in the tested Reynolds number regime. A thin body with a minimum top area is proven to be a good shape for reducing drag at the high angles of attack,** $\alpha = 45\,\mathrm{deg}$ **and** $\alpha = 90\,\mathrm{deg}$**. It was identified that general recommendations for drag reduction on full scale helicopters also work at the lower Reynolds numbers, but primarily at low angles of attack.**

I. Introduction and aims

The use of micro aerial vehicles (MAVs) has escalated in the last decade and is expected to grow further with sales projected to reach $82 billion USD by the end of the decade [1]. MAVs operate in the lower part of the atmospheric boundary layer (ABL) [2] and are susceptible to varying wind and gusts. While large aircraft fly in all but the most extreme wind conditions, MAVs are limited by a maximum operational speed around 20 m/s. Furthermore, MAVs operate in a low Reynolds number regime, typically in the range $1 \times 10^3 < Re < 1 \times 10^5$ [3]. In this regime the airfoil efficiency is greatly reduced and the drag increases due to the viscous effects [4]. Research has focused on designing the best possible airfoils and rotors for these conditions [5–7]. Ref [8] investigated the effects of varying turbulence intensities and integral length scales on the airfoils, but few have focused on the fuselages of MAV helicopters. This calls for better designed MAV bodies for at least two reasons, increased flight time with less drag and increased operational regime due to better gust response.

A considerable amount of work has been done on drag reduction and prediction for large scale helicopters, see e.g [9–17]. The key points identified will be given here. Rounding of surfaces is beneficial, specifically the ratio of the corner radius R_c of the nose to the width of the body w should be greater than 0.1. A rounded cross section is also favorable to reduce the cross flow effect at cruise. The rear fuselage where the main body tapers to the tail boom is especially important. Helicopters with an up-sweep in the rear can experience two different phenomena: the traditional bluff body flow with cross stream eddies, and streamwise vortices [17]. These vortices increase the drag and as a second penalty generate a downward facing force.

The varying turbulence intensities in the ABL will influence the drag genereated by the MAV. Turbulence in the ABL can be characterized by the turbulence intensity and the integral length scale. The integral length scale can vary from under a meter to several meters, significantly bigger than any MAV [18]. Studies have shown that the turbulence intensities can vary from 5% to 40% relative to the moving vehicle, depending on wind speeds and the velocity of the MAV [18, 19]. Forces on the MAV are influenced in two main ways by turbulence: it produces unsteady buffeting loads, and alters the mean flow field due to the complex interactions between the flow and the turbulence [20]. For example, the increase of turbulence intensity on a sphere in a Reynolds number regime $2.2 \times 10^4 < Re < 8 \times 10^4$ reduces its drag [21]. Interestingly, the drag is also decreased with a decreasing turbulent length scale.

The problem of drag reduction can be expressed as an optimization problem. The increase of computational power and significant cost savings of using CFD in a development process has lead to the development of many CFD-software packages. This in turn has lead to an increase in CFD-based optimization. Within optimization, (an) objective(s) of interest is decided, e.g a lift and/or drag coefficient. This objective is then minimized or maximized according to the desired criteria. Optimization problems can be either single objective optimization (SOO) or multi objective

---

[*] Master student, NTNU, Department of Energy and Process technology, Kolbjørn Hejes vei 1D, 7034 Trondheim, Norway

optimization (MOO). When there is little knowledge about the importance of each objective, a MOO approach can be used [22] which results in a Pareto frontier. If a priori knowledge is available, e.g that lift is more important than drag, the different objectives can weighted and casted into a SOO problem. CFD-based optimization is split into two main categories: stochastic and deterministic [23]. Examples of stochastic algorithms are genetic algorithms[24, 25]. They mimic nature evolution process and find an global optimum/minimum at a large computational cost. Deterministic algorithms typically start with a fixed geometry and then alter it as the optimization moves forward [26]. Usually, a deterministic approach is based on derivatives, hence the computational cost is linked to how efficiently derivatives can be computed. Using a simple finite difference method is computationally very expensive, whereas a more efficient procedure is the adjoint method [27].

The main drawback for both stochastic and deterministic algorithms is that both need an automatically altered geometry. A parameterization of the MAV body is beyond the scope of this work and hence simple, manual designed bodies made with CAD are used instead. We suggest an inherently simple, yet structured optimization method. We start with a simple body of appropriate size and shape, within the constraints and calculate the Figure of Merit (F_M) defined as follows

$$F_M = \sum_{i=0}^{k} C_{D,i} \cdot \zeta_i, \tag{1}$$

where $C_{D,i}$ is the drag coefficient at a given angle of attack and ζ_i are some chosen weights greater than zero who fulfill the following constraint

$$\sum_{i=0}^{k} \zeta_i = 1. \tag{2}$$

Furthermore, the drag coefficient is given as

$$C_D = \frac{D}{\frac{1}{2}\rho A U_\infty^2} \tag{3}$$

where D is the drag force tangential to the incoming flow, ρ is the density, A is the frontal area of the first body and U_∞ the incoming mean velocity.

The aim of this work is to execute a simple optimization strategy for MAV helicopter body optimization where the objective is to minimize F_M and investigate the drag coefficient of different helicopter body shapes experimentally to shed light on the flow physics and validate the computational approach. We will start with a basic body constructed from two rectangular cuboids, then implement the advised strategies for drag reduction and finally introduce some new concepts. The MAV will be simulated in the CFD study at two angles of attack, namely $\alpha = 0$ deg and $\alpha = 45$ deg, where $\alpha = 0$ deg points the nose directly into the flow and a positive angle is downwards. In the experimental campaign we will do measurements for $\alpha = 0$ deg, $\alpha = 45$ deg and $\alpha = 90$ deg to shed greater light on the flow physics and validate the CFD model. The helicopter bodies considered in this work, must have space for at least two cameras, battery, motors as well as a small on-board computer. Formally, the length is set to be $l = 180$ mm, the width $30\,\text{mm} \leq w \leq 40\,\text{mm}$ and the height h, $30\,\text{mm} \leq h \leq 40\,\text{mm}$. Furthermore, either the height or the width must be 40 mm to accommodate for two cameras. The transition from main body to tail must be located around the center at $x = 90$ mm.

In section II, we will discuss the numerical set-up and the proposed optimization method. In section III we discuss the experimental set-up and in section IV the computational and experimental results are presented with a discussion. Finally in section V we conclude.

II. Numerical methods

MAVs are governed by the incompressible Navier-Stokes equations, specifically the continuity equation

$$\int_A \mathbf{u} \cdot \mathbf{n} dA = 0, \tag{4}$$

and the momentum equation

$$\frac{\partial}{\partial t} \int_V \mathbf{u} dV + \int_A \mathbf{u}(\mathbf{u} \cdot \mathbf{n}) dA = -\frac{1}{\rho} \int_A p \cdot \mathbf{n} dA + \int_A \nu (\nabla \mathbf{u}) \cdot \mathbf{n} dA, \tag{5}$$

where V is the control volume, A the surface that surrounds the volume V, ρ is the fluid denisity, p the pressure, $\mathbf{u} = [u_x, u_y, y_z]$ the velocity vector, where u_x, u_v and u_z are the velocity components in the $x-$, $y-$ and $z-$ directions respectively, $\mathbf{n}$ the unit normal vector to the area element dA, and ν the kinematic viscosity. For the problem at hand we use the steady Reynolds averaged Navier-Stokes (RANS) equations, see e.g [28].

The Reynolds stress term in the RANS-equations is approximated through the Boussinesq hypothesis [28] which relates the term to the mean flow quantities and a turbulent viscosity. The turbulent viscosity is modelled with the Spalart-Allmaras [29] turbulence model, see Appendix A.A for further details. The Spalart-Allmaras model is chosen because of its applicability to external aerodynamics and the fact that it is integrated into the adjoint-optimization method in the OpenFOAM® solver *adjointOptimizationFoam*, described in [27].

To solve the equations we use the known and widely accepted finite volume solver OpenFOAM® [30] version 2006. The steady state SIMPLEC-algorithm [31] is used with second-order discretizations for all spatial derivatives and a second-order upwind-biased scheme for the convective terms, see e.g [32, 33] for how to compute the fluxes. The linear systems of equations are solved with a geometric algebraic multigrid method for the pressure equation, and the pre-conditioned bi-conjugate stabilized method [34], with the simplified diagonal-based incomplete lower-upper for asymmetric matrices pre-conditioner [34], for all other variables. The convergence criterion for the linear systems of equations is set to the tolerance $\epsilon < 1 \times 10^{-8}$, and a minimum of three iterations were ran for all systems.

The mesh is generated with OpenFOAM® utility *snappyHexMesh*, see [35] for details. It creates an unstructured hexahedral dominated mesh for use in complex geometries. The domain is depicted in Fig. 1 and its dimensions are $2.6\,\mathrm{m} \times 1.44\,\mathrm{m} \times 1.44\,\mathrm{m}$ in the x,y and z direction respectively corresponding to $65w \times 36w \times 36w$ in a width-normalized coordinate system, with the MAV situated at 0.88 m from the flow inlet in the $x-$direction and centered in the $y-z$ plane.

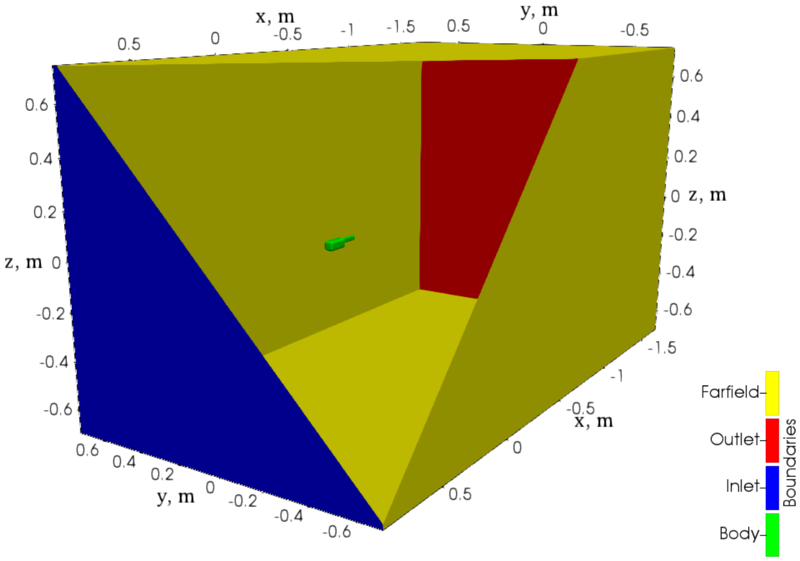

Fig. 1 Numerical domain used in OpenFOAM® for all simulations.

The boundary conditions are listed in Table. 1. For the transported variable $\tilde{\nu}$ the boundary condition is chosen according to recommendations by NASA [36]. The turbulent viscosity ν_T is calculated for all boundaries.

Table 1 Boundary conditions used for all simulations in OpenFOAM®. The inlet velocity components are adjusted according to the angle of attack.

Variable	Inlet	Outlet	Body	Farfield
U	fixed value, 10 m/s	zero gradient	no-slip	freestream, 10 m/s
p	fixed value, $0\,\mathrm{m^2/s^2}$	fixed value, $0\,\mathrm{m^2/s^2}$	zero gradient	fixed value, $0\,\mathrm{m^2/s^2}$
$\tilde{\nu}$	freestream, $4.44 \times 10^{-5}\,\mathrm{m^2/s}$	freestream, $4.44 \times 10^{-5}\,\mathrm{m^2/s}$	fixed value, $0\,\mathrm{m^2/s}$	freestream, $4.44 \times 10^{-5}\,\mathrm{m^2/s}$

An estimation of the discretization error was performed using the grid convergence method described in [37]. The boundary conditions listed in Table. 1 were used for the simulations. In Fig. 2 the convergence of the simulation on the finest mesh is depicted. The results and parameters from the grid convergence method are reported in Table. 2. The estimated discretization error is estimated to 0.78% for the mesh with 6.75 million cells. This does not, however, account for modelling errors. A layer refinement is used on the surfaces ensuring a $\max(y^+) < 6$ for all simulations. Small perturbations in the boundary condition had a negligible effect on the monitored variable C_D. Boundary dependence was tested by approximately doubling the size of the domain in all directions, with a slight change in the monitored variable C_D in the third digit, hence it was concluded that the domain is large enough for the boundaries not to influence the solution. The mesh used further on is depicted in Fig. 3.

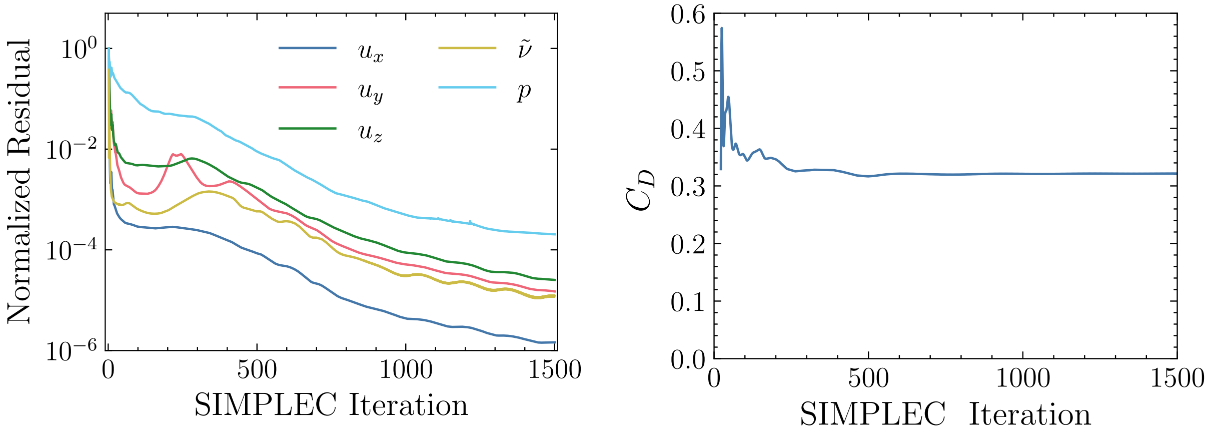

(a)

(b)

Fig. 2 Decreasing residuals converged by at least three magnitudes with a stabilized monitored variable, C_D, indicating iterative convergence of the numerical simulation. Notice that C_D is unchanged from iteration 500. A further 1000 iterations were run to confirm that C_D was fixed.

Table 2 Variables and results from the grid convergence study. N is the cell count, r_{xy} is the average cell size from mesh y divided by the average cell size from mesh x. p the apparent order of the simulation and GCI the estimated discretization error. See section A.B in the appendix for a full description of the method used.

Variable	Mesh 1	Mesh 2	Mesh 3
N	6747371	3155349	1212784
r_{21}	1.288		
r_{32}		1.375	
C_D	0.318	0.319	0.321
p	1.669		
$C_{D,ext}^{21}$	0.315		
GCI_{fine}^{21}	0.78%		

The numerical model was tested on a sphere for a Reynolds number $Re \approx 27000$ using the same mesh settings as described above. The resulting drag coefficient from the study is $C_D = 0.45$, which is comparable with the standard curve for drag on spheres reported in [21]. This is an indication that the model can be used with satisfactory results for bluff bodies in low Reynolds numbers.

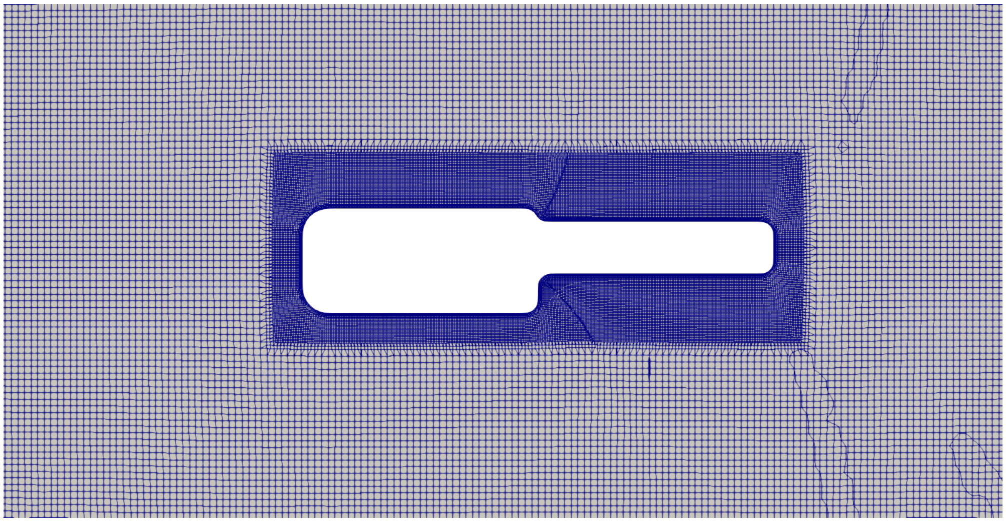

Fig. 3 Slice in the $x - z$ plane of the mesh with 6.75 million cells around the object of interest. The radial lines are visualization errors rather than mesh errors.

To optimize the MAV helicopter body we use a simple optimization process defined as following:

1) Create a simple initial body within the design constraints
2) Choose a set of angles of attack/inflow conditions and a set of corresponding weights fulfilling Eq. (2)
3) Calculate the Figure of Merit for the initial body using Eq. (1)
4) Create two new bodies from the initial body based on best practices, literature or recommendations from the CFD software
5) Calculate the Figure of Merit for the two new bodies using Eq. (1)
6) From all bodies tested pick the one with the best Figure of Merit and create two new bodies
7) Repeat step 5 and 6 until a satisfactory result is reached
8) If necessary, restart the process with a new initial body.

This method does not guarantee a global minimum/maximum, however it will yield an improved performance. For the specific problem we have chosen the angles of attack α to be

$$\alpha = [0\,\text{deg}, 45\,\text{deg}] \tag{6}$$

with the weights given as

$$\zeta = [0.25, 0.75]\,. \tag{7}$$

The chosen weights emphasizes the drag at higher angles of attack. Both simulations and experiments are performed without a rotor, the higher weight of the high angle of attack is therefore chosen to mimic the influence of the main rotor. It is here noted that rotor-fuselage interactions likely will have a big effect on the performance, however we disregard it when only investigating the drag, see [13] for details.

III. Experimental Techniques

Force measurements were conducted on a set of five different MAV fuselages. The forces were measured at three different angles of attack, 0 deg, 45 deg and 90 deg, where at $\alpha = 0$ deg the nose of the MAV points directly into the flow and at $\alpha = 90$ deg the nose points into the ground. Three angles were chosen to more light on flow physics and the drag as a function of angle of attack. Experiments were performed at width-based Reynolds numbers from $Re = 16000$ to $Re = 41000$, with a width of 40 mm. A majority of the measurements were performed at $Re = 23000$ and $Re = 27000$, corresponding to a length based Reynolds number of $Re = 103500$ and $Re = 121500$, which will be demonstrated to be within the Reynolds number independent regime.

A. Experimental Set-up

The experiments were conducted in the large closed loop wind tunnel at the Norwegian University of Science and Technology (NTNU) in Trondheim, Norway. The wind tunnel is capable of reaching homogeneous flow speeds from up to 20 m/s and has a working section of 11.1 m × 2.7 m × 1.8 m in the x, y, z direction respectively were x is the flow direction. In a clean flow the turbulence intensity, $u_x^{'}/u_x$, where $u_x^{'}$ is the velocity fluctuation and u_x the mean velocity in the x-direction, was measured to be 0.72% using cross wire and constant temperature anemometery. Figure 4 shows a homogeneity scan of the test section used in the wind tunnel, confirming that the flow is homogeneous across the plane the set-up is mounted in. The models were mounted on a rig, depicted in Fig. 5, in the center of the test chamber at $z = 1030$ mm in the upright position. The rig consists of a sting that rotates and allows for different angles of attack with increments of 22.5 deg. The model was mounted on a sting covered by a circular cylinder with a splitter plate to limit the vortex shedding. Inside the cylinder the measurement equipment was mounted between the rotatable end mount and a carbon fiber rod with a diameter of 8 mm, which connected the load cell to the model. This setup corresponded to a blockage ratio in the wind tunnel of approximately 1.87 %. The models that were measured were all 180 mm long and had variable width and height between 30 mm and 40 mm. The models were 3D-printed using a Prusa I-3 MK2 3D-printer and sanded with a 200 grit 3M sand paper.

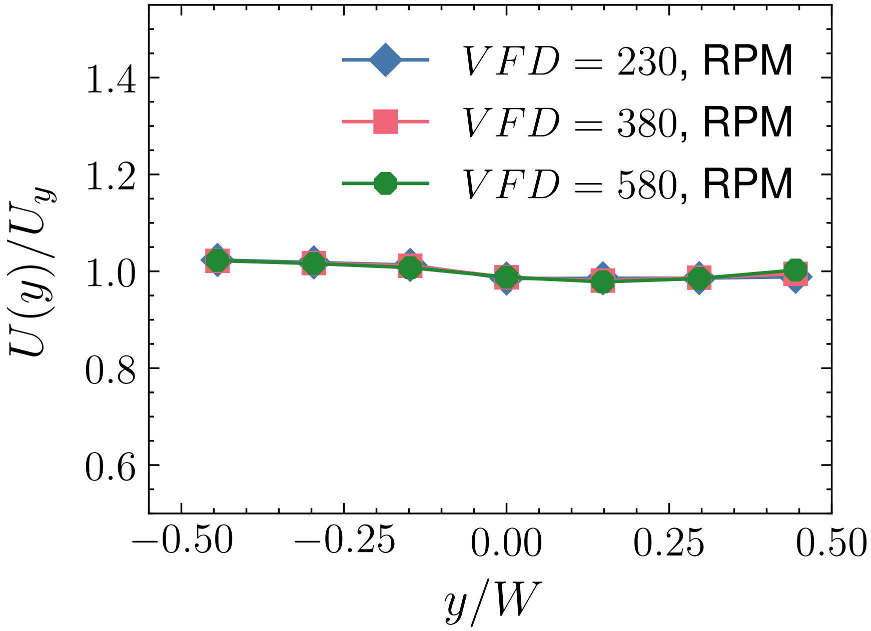

Fig. 4 Homogeneity scan of the test section in the wind tunnel measured with cross wires. The fan settings $VFD = 230RPM$ and $VFD = 580RPM$ corresponds to the lowest and highest fan speed settings used for the experiments. W is the width of the test section. $U(y)$ is the local mean velocity at different y-locations, and U_y is the spanwise average mean velocity. A homogeneous flow is observed across the test section. Data courtesy of Leon Li.

B. Force Measurements

The forces were measured with a six axis ATI-17-E Nano force transducer with SI-12-0.12 calibration. The measurement resolution is reported to be 1/320 N in all directions for the forces and the load cell calibration is traceable to the National Institute of Standards and Technology, hence the load cell was not calibrated by us. To limit the temperature drift, zero-measurements were taken post and prior to all experiments, ensuring that the sensor did not drift. In addition, measurements for two of the models were performed at two different days, ensuring the measurements were set-up independent. The force measurements were sampled at 200 Hz for 60 s per measurement. A Fourier transformation revealed oscillations at a frequency of 18 Hz. The frequency peak was independent of the Reynolds number and hence not related to the vortex shedding, but rather concluded to be structural related.

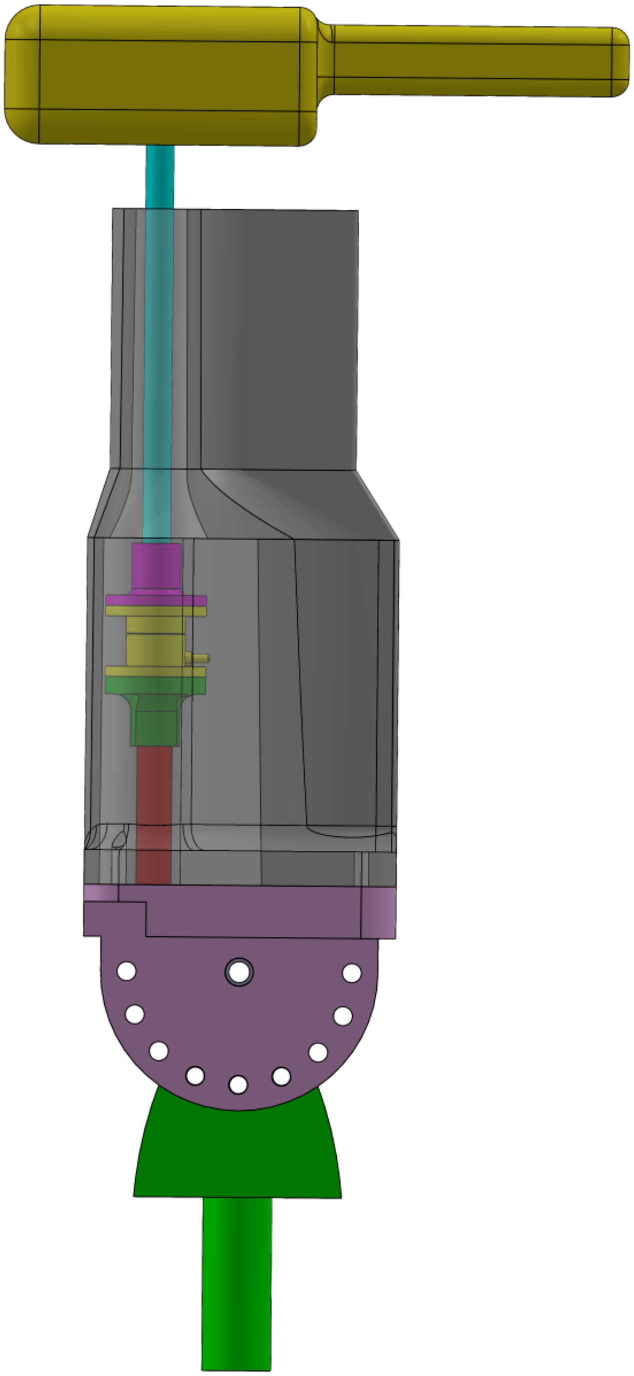

Fig. 5 Schematic of the experimental set-up. In yellow between the sting and the rotatable mount the load cell ATI Nano-17 is located. In purple at the bottom the rotatable mount is located and in grey the cylinder with a splitter plate shielding the sting from the flow.

IV. Results and Discussion

In this section, we will first illustrate the numerical results computed with OpenFOAM® and the optimization of the body shape, then we describe the results from the experiments and finally we conclude with the comparison between the two approaches.

A. CFD based optimization

The optimization of the fuselage starts out with the initial body "Basic" depicted in Fig. 6. All simulations are performed at a width based Reynolds number $Re \approx 27000$. CFD-simulations from $Re = 13000$ to $Re = 33000$ indicated the drag was Reynolds number independent. For each generation the model with the best F_M was chosen as *parent* for the next generation, creating two new models (*children*). If none of the *children* performed better than their *parent*, the *parent* model was used again to create a new generation. The results from the optimization is listed in Table 3, with the resulting shapes shown in Fig. 7. Fuselage 2B and 4A depicted in Fig. 7d and Fig. 7g respectively, which are thinner than the fuselage "Basic", performed best with both 2B and 4A achieving $F_M = 0.69$.

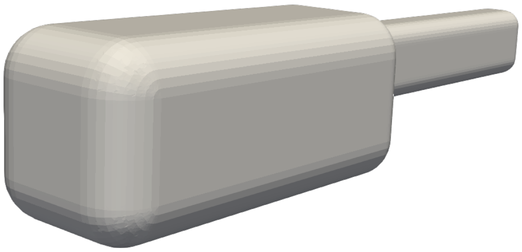

Fig. 6 The model "Basic" used as a starting point for the optimization process. This model is used further on as a baseline in the experimental campaign.

In general, all the models perform quite well at $\alpha = 0$ deg with a minimum $C_D = 0.14$ and a maximum $C_D = 0.23$, substantially lower than the "Basic" fuselage depicted in Fig. 6. All models use the same projected frontal area to compute C_D, while the models 2B, 4A and 5B have a frontal area that is 25% smaller than the frontal area of "Basic". This would yield an $C_D = 0.28$ for model 2B, which is the worst performance. However, the model is within the design constraints and it is therefore left as a note. The relative low C_D values obtained can be physical as some of the bluff bodies are relatively streamlined. Especially, model 2A (Fig. 7c) is a streamlined body, that generates little form drag and has an estimated $C_D = 0.14$. The numerically calculated drag coefficients, C_D, are very low compared with the experimental ones. This issue will be addressed in section IV.C.

The deciding factor in all the simulations is the drag coefficient at $\alpha = 45$ deg. This angle is greater emphasized in the weighting as the flows for helicopter comes from above or some angle between the horizontal axis and the the vertical axis. Spanning from $C_D = 0.85$ to $C_D = 1.46$ considerable improvements can be made by selecting the right fuselage. All models experience a substantial reverse flow underneath the bodies at $\alpha = 45$ deg, visualized in Fig. 8. One can observe that model 2B, depicted in Fig. 8h, has the least reverse flow both in magnitude and area compared to the other fuselages. At the front of the models it is observed that models with a sharp edge, e.g "Basic" in Fig. 8b, has a wider separation region underneath the body compared to the models with a rounder edge, e.g model 1A in Fig. 8d. This is consistent with theory.

The results can be split into three main categories, $C_D > 1.3$, $1.0 < C_D < 1.3$, and $C_D < 1$. The models with $C_D > 1.3$ are all characterised by a large projected surface area in the vertical direction, essentially making them bluff bodies for flow coming from above or beneath. This geometry creates a large form-drag from the pressure loss, as well a large recirculating bubble beneath the model, depicted in Fig. 8b. Fuselage 5B and "Basic" are similar models, except that the height of model 5B is 30 mm while "Basic" has height of 40 mm. The lower height results in a drag increase, consistent with [38] which showed that an increase of length in the stream wise direction of cuboids reduces the drag. In general, tapering increases the projected area in the vertical direction and yields an increased drag compared to either fuselages with rounded surfaces or without tapering. Tapering the body to the tail is therefore beneficial when flying forward at high speeds with low angles of attack, but for vertical flight or hovering the benefit of this configuration is negligible. The two highest performing models with respect to desired criteria are the most elementary models with a smaller width, model 2B and 4A depicted in Fig. 7d and Fig. 7g respectively, both with a F_M of 0.69, with a leading edge slightly angled backwards. These models have the smallest vertical projected surface area, and their bodies are fairly streamlined and the resulting drag is minimized.

Table 3 Results from the CFD optimization with the best models marked in bold.

Iteration	Model	Description	C_D, $\alpha = 0$ deg	C_D, $\alpha = 45$ deg	F_M	Figure
0	Basic		0.32	1.39	1.12	Fig. 6
1	1A	Rounded	0.23	1.14	0.92	Fig. 7a
1	1B	Tapered	0.18	1.32	1.04	Fig. 7b
2	2A	Rounded with taper	0.14	1.32	1.03	Fig. 7c
2	**2B**	Thin	0.21	0.85	0.69	Fig. 7d
3	3A	Thin with thinner tail taper	0.19	1.03	0.82	Fig. 7e
3	3B	Thin with thinner tail rounded	0.22	1.04	0.84	Fig. 7f
4	**4A**	Thin angled top	0.21	0.85	0.69	Fig. 7g
4	4B	Thin with tail taper	0.20	1.03	0.82	Fig. 7h
5	5A	Thin curved top	0.20	0.95	0.76	Fig. 7i
5	5B	Wide	0.22	1.46	1.15	Fig. 7j

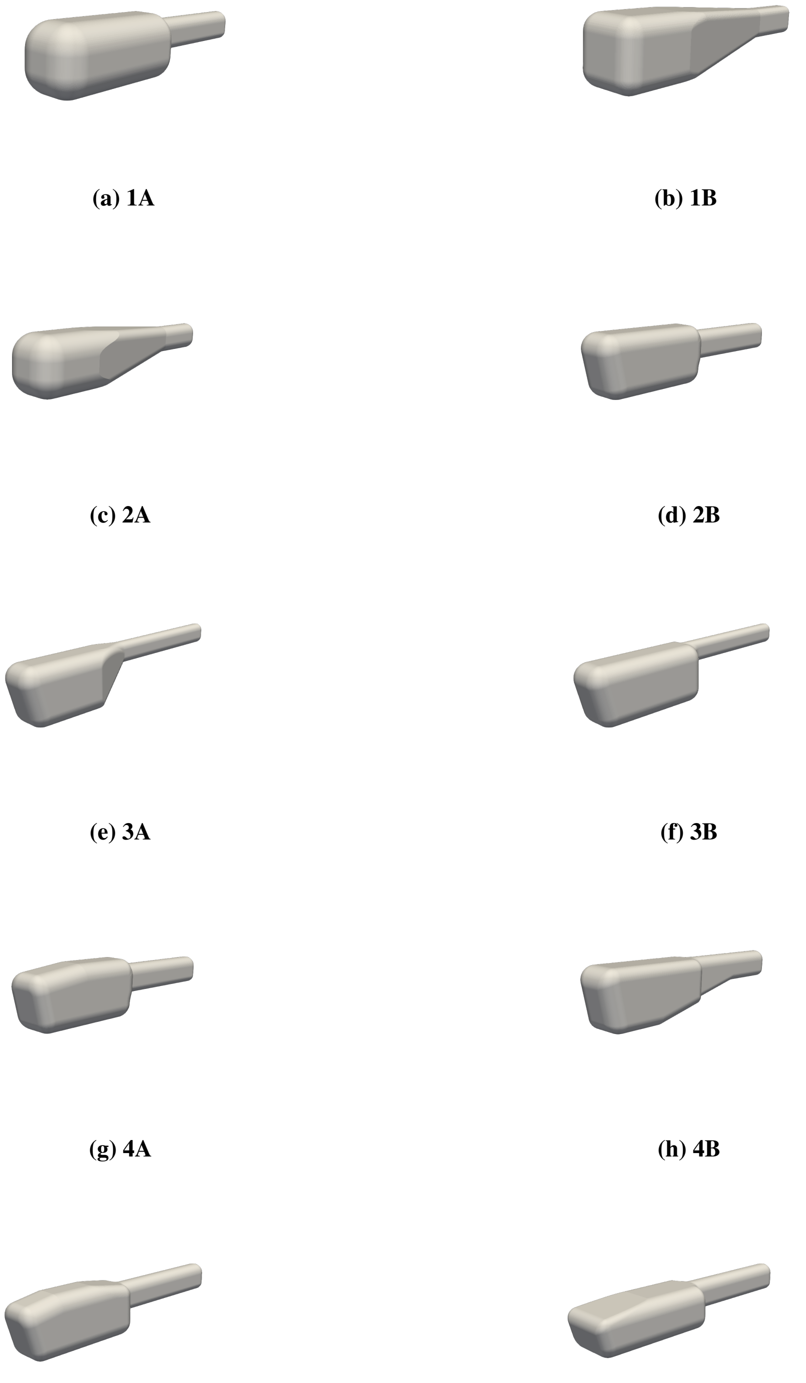

(a) 1A

(b) 1B

(c) 2A

(d) 2B

(e) 3A

(f) 3B

(g) 4A

(h) 4B

(i) 5A

(j) 5B

Fig. 7 The models investigated and tested in OpenFOAM® throughout the optimization process. A subset of these models are later used for the experimental campaign. The sub captions states the name of the model, see also Table. 3 for a further description.

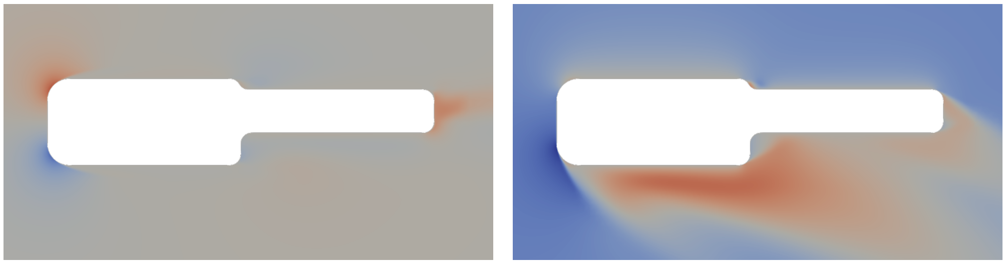

(a) Basic (b) Basic

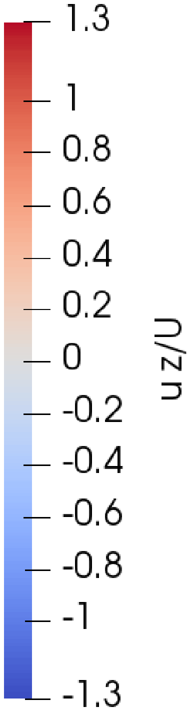

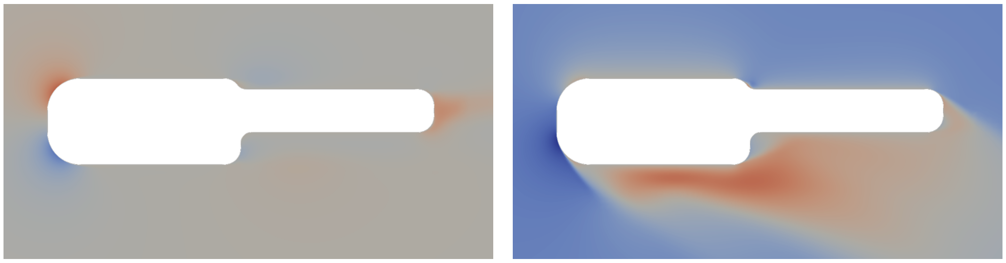

(c) 1A (d) 1A

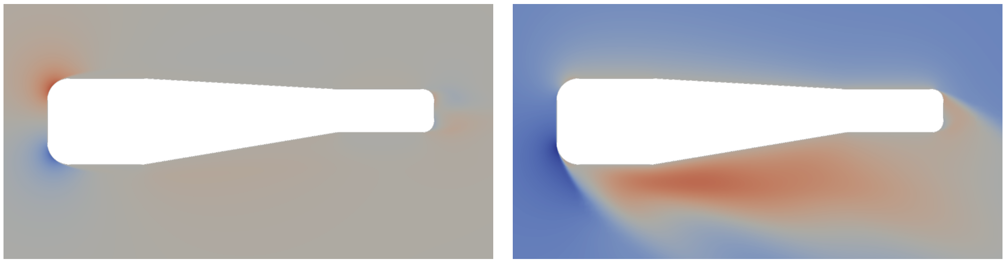

(e) 1B (f) 1B

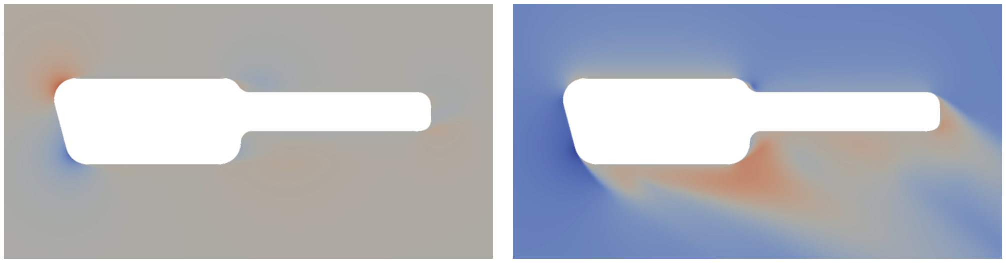

(g) 2B (h) 2B

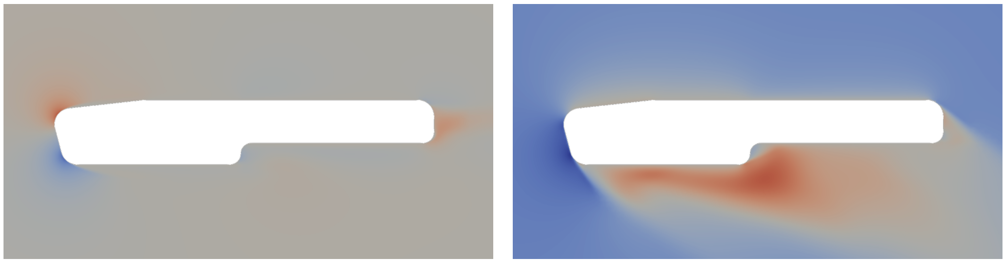

(i) 5B (j) 5B

Fig. 8 **Velocity field in the $x - z$ plane on five models computed with OpenFOAM®. The color map represent the vertical velocity component u_z/U, where U is the free stream velocity. In the left column we have $\alpha = 0\,\text{deg}$ and on the right hand side $\alpha = 45\,\text{deg}$. A large region of reverse flow is observed at $\alpha = 45\,\text{deg}$. The sub captions states the model name.**

B. Experimental results

Experiments were conducted on the models "Basic" (Fig. 6), 1A (Fig. 7a), 1B (Fig. 7b), 2B (Fig. 7d) and 5B (Fig. 7j). "Basic" was chosen as it was the starting point and the simplest model. Model 1A and 1B were chosen as both tapering the tail to fuselage and rounding corners are listed in the literature on how to reduce the drag. Finally model 2B and 5B were chosen because these were the best and the worst models from the optimization routine. Model 2B and 4A are very similar, hence 4A was disregarded.

The effect of the Reynolds number on the C_D was investigated on three models, "Basic", 1B and 2B. It is depicted in Fig. 9 and shows that the C_D is independent of the Reynolds number within the given range. Model 2B (Fig. 7d) outperforms the other models, as shown in Fig. 10. At $\alpha = 0$ deg fuselage 5B (Fig. 7j) performs marginally better, however this performance deteriorates as the angle of attack increases. At $\alpha = 90$ deg we find three distinct groups. First the three models with the highest drag coefficient, which all have a similar top surface, large and flat, making them comparable to a bluff body. fuselage 1B has the biggest surface area on top and hence it is sensible that this results in the highest drag at the given angle. Secondly there is model 1A (Fig. 7a) where the effect of rounding the corners can be observed as a reduction in the drag. Finally, model 2B (Fig. 7d) which has the least surface area on top and is best by a significant margin.

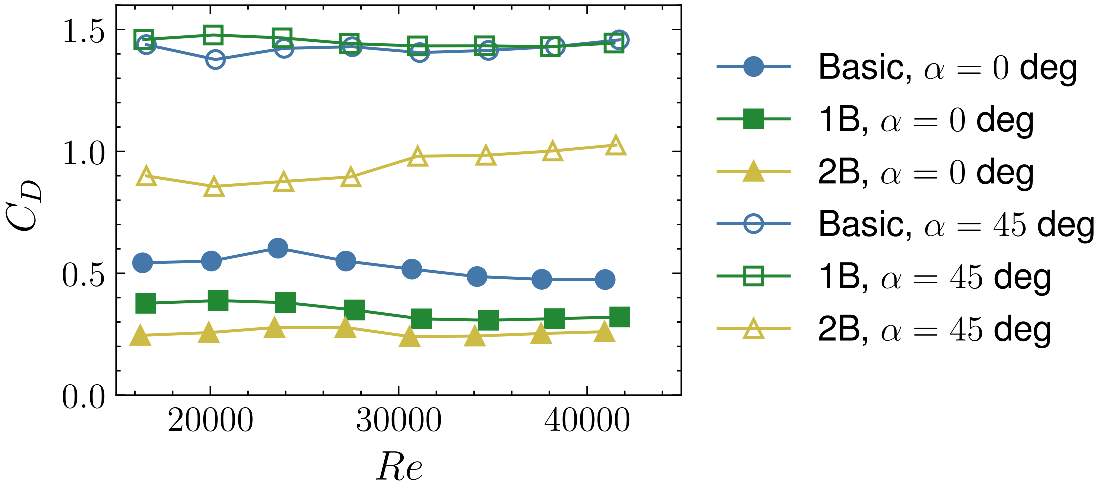

Fig. 9 Investigation the effect of the Reynolds number on the drag coefficient C_D at two angles of attack. For $\alpha = 0$ deg the drag from from the sting is subtracted, corresponding to approximately $C_D = 0.2$.

C. Validation of the numerical model

We noticed significant discrepancies in the results from CFD simulations and experiments. In Table 4 and 5 we report the experimental versus computational drag coefficients at $\alpha = 0$ deg and $\alpha = 45$ deg respectively. The relative percentage difference, defined as the absolute difference divided by the experimental C_D, is as high as 50% for model 1B in the horizontal case ($\alpha = 0$ deg). This is likely due to the miscalculation of the skin friction in the CFD-model. The skin friction corresponds to approximately 15% of the drag on model 1B at $\alpha = 0$ deg in the CFD study. For an airfoil, skin friction accounts for approximately $70 - 90\%$ of the total drag. Fuselage 1B falls in between the categories of bluff and streamlined bodies, thus it is plausible that the skin friction contribution should be higher than the one measured in CFD simulations. For low Reynolds numbers there are known problems with the calculation of skin friction when using Spalart-Allmaras, which Spalart and Garbaruk, [39], has tried to fix with a change in the C_{w2} constant in the model. They have suggested changing the constant to a function based on the boundary layer thickness. An error in the estimation of the drag coefficients is also reported in [40] who used the spalart-Allmaras model to predict lift and drag on airfoils with the solver TURNS2D. A second source of errors is the surface roughness of the models. The computational model has zero surface roughness, while experimental fuselages are sanded with grit 200 sand paper. Simulations were also performed with k-ω SST with a turbulence intensity of 2% for the models "Basic" and 1B, however, the drag coefficients obtained were approximately the same.

As shown in Table. 5 the trend from the CFD-analysis is exactly the same as for experiments at $\alpha = 45$ deg. This

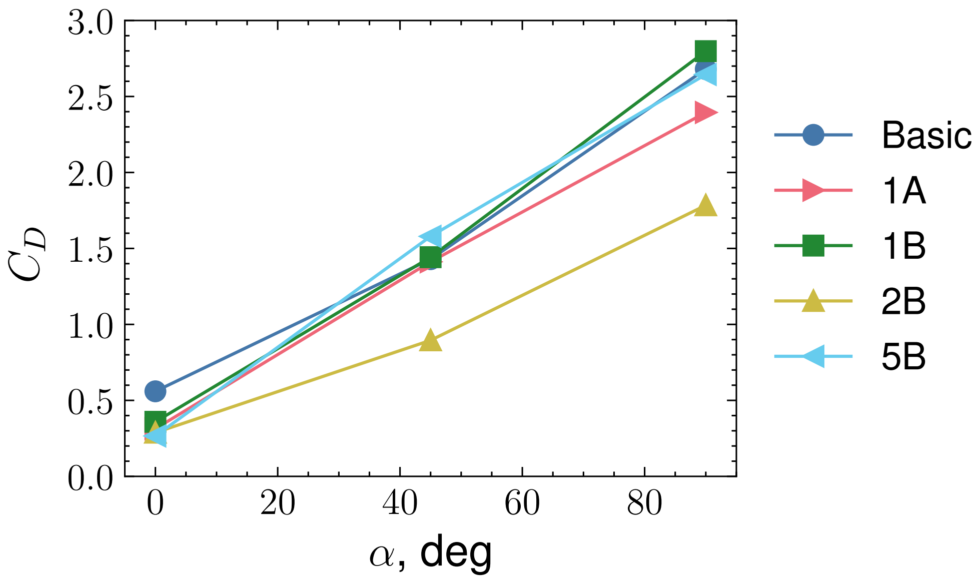

Fig. 10 Drag coefficients from experiments at $Re \approx 27000$ versus angle of attack. For $\alpha = 0$ deg and $\alpha = 90$ deg the drag from from the sting is subtracted, corresponding to approximately $C_D = 0.2$.

Table 4 Comparison between experimental values and computational drag coefficients at $\alpha = 0$ deg.

Model	C_D, Experimental	C_D, CFD	Absolute Difference	Percentage Difference
Basic	0.56	0.32	0.24	42.8%
1A	0.31	0.23	0.08	25.0%
1B	0.36	0.18	0.18	50.0%
2B	0.28	0.21	0.07	25.0%
5B	0.26	0.22	0.04	15.4%

indicates that the CFD-analysis predicts accurately which geometries performs better. The average difference between CFD and the experiment is 8.6% for the case of $\alpha = 45$ deg, which is deemed satisfactory. For the $\alpha = 0$ deg the average difference between CFD and the experiment is 31.6 % and the trend is falsely predicted. Fuselage 1B performed best in the CFD study at $\alpha = 0$ deg, however in the experiments model 5B performs better at this angle. It is noted that the differences in C_D from the CFD study at $\alpha = 0$ deg are minor. When compared with the experiments, these minor differences are likely within the uncertainty of the measurements of the experiments, making it hard to conclude.

Table 5 Comparison between experimental values and computational drag coefficients at $\alpha = 45$ deg

Model	C_D, Experimental	C_D, CFD	Absolute Difference	Percentage Difference
Basic	1.42	1.38	0.04	2.8%
1A	1.41	1.14	0.27	19.1%
1B	1.44	1.32	0.12	8.3%
2B	0.85	0.89	0.04	4.7%
5B	1.58	1.46	0.12	7.9%

In the optimisation with the weighting function chosen, the C_D at $\alpha = 45$ deg matters more. Table. 6 shows the F_Ms computed from CFD and experiments. The average difference between CFD and the experiments is 9.6% for the F_M, yielding a quite precise estimate. The ranking of all models are exactly the same from the experiments and the CFD, meaning the CFD accurately predicts the trend for our given F_M.

Table 6 Comparison between the Figure of Merits computed from CFD and Experiments.

Model	F_M, Experimental	F_M, CFD	Absolute Difference	Percentage Difference
Basic	1.21	1.12	0.09	7.4%
1A	1.13	0.92	0.21	18.6%
1B	1.17	1.04	0.13	11.1%
2B	0.71	0.69	0.02	2.8%
5B	1.25	1.15	0.10	8.0%

V. Conclusions

A MAV has been optimized with respect to drag using an inherently simple optimization strategy with CFD-tools. The optimization lead to a MAV design with a 38% decrease in the F_M compared to the original model. To validate the CFD results, experiments have been performed on a subsample of the models designed in the optimization routine. The trends identified are promising, but when skin friction is important the CFD-model underestimates the drag. In a form drag dominated regime the CFD and the experiments are in good agreement. This is a reminder of why it is always important to validate CFD results. Caution must be taken when applying the CFD-model, especially in a skin-friction dominated regime when the drag coefficient is of interest.

Analysis of the fuselages by both CFD and experiments has shown that rounding the edges and minimizing the top area of the MAV is beneficial to drag reduction when the MAV is subjected to flows coming from above, such as the rotor wake or during climbing flight. For a flow regime dominated by flow from the front rounding the edges is still beneficial, as well as tapering the body to the tail, in an effort to reduce the flow separation.

The optimization routine is in good agreement with experimental investigation, yielding the same trend in the ranking of helicopter models. Model 2B, Fig. 7d, performed the best both in CFD simulations and wind tunnel experiments with a F_M of 0.69 and 0.71 respectively. For a form drag dominated regime the optimization routine shows promising result, and can likely be used as a part of MAV helicopter design process. It is important to be aware of the flaws in the model, especially at the lower angles of attack. It was also observed that it is beneficial to minimize the top area at the cost of the side area when the objective is to minimize drag and increase the flight time. In this study we have not taken into account wind coming from the side, which likely will have an influence on the drag. General recommendations for helicopter drag reduction works also at lower Reynolds number, however they perform best at low angles of attack.

The validation is done solely through drag estimations, to further increase the reliability of the CFD model, additional flow field measurements should be carried and compared.

References

[1] Ohio University, “The Benefits and Challenges of UAVs,” , 2020. URL `https://onlinemasters.ohio.edu/blog/the-benefits-and-challenges-of-uavs/`.

[2] Watkins, S., Milbank, J., Loxton, B. J., and Melbourne, W. H., “Atmospheric winds and their implications for microair vehicles,” *AIAA Journal*, Vol. 44, No. 11, 2006, pp. 2591–2600. https://doi.org/10.2514/1.22670.

[3] Lakshminarayan, V. K., and Baeder, J. D., “Computational investigation of microscale coaxial-rotor aerodynamics in hover,” *Journal of Aircraft*, Vol. 47, No. 3, 2010, pp. 940–955. https://doi.org/10.2514/1.46530.

[4] Cleaver, D. J., Wang, Z., Gursul, I., and Visbal, M. R., “Lift enhancement by means of small-amplitude airfoil oscillations at low Reynolds numbers,” *AIAA Journal*, Vol. 49, No. 9, 2011, pp. 2018–2033. https://doi.org/10.2514/1.J051014.

[5] Mueller, T. J., and DeLaurier, J. D., “Aerodynamics of small vehicles,” *Annual Review of Fluid Mechanics*, Vol. 35, 2003, pp. 89–111. https://doi.org/10.1146/annurev.fluid.35.101101.161102.

[6] Torres, G. E., and Mueller, T. J., “Low-aspect-ratio wing aerodynamics at low reynolds numbers,” *AIAA Journal*, Vol. 42, No. 5, 2004, pp. 865–873. https://doi.org/10.2514/1.439.

[7] Okamoto, M., and Azuma, A., “Aerodynamic characteristics at low reynolds numbers for wings of various planforms,” *AIAA Journal*, Vol. 49, No. 6, 2011, pp. 1135–1150. https://doi.org/10.2514/1.J050071.

[8] Ravi, S., Watkins, S., Watmuff, J., Massey, K., Petersen, P., Marino, M., and Ravi, A., “The flow over a thin airfoil subjected to elevated levels of freestream turbulence at low Reynolds numbers,” *Experiments in Fluids*, Vol. 53, No. 3, 2012, pp. 637–653. https://doi.org/10.1007/s00348-012-1316-2.

[9] Montana, P. S., “Experimental investigation of three rotor hub fairing shapes,” Ph.D. thesis, Naval Ship Research and Development Center Bethesda, Maryland, 1975.

[10] Keys, C. N., and Wiesner, R., “Guidelines for Reducing Helicopter Parasite Drag,” *Journal of the American Helicopter Society*, Vol. 20, No. 1, 1975, pp. 31–40.

[11] Chaffin, M. S., and Berry, J. D., “Navier-Stokes and Potential theory Solutions for a Helicopter fuselage and Comparison with Experiment,” Tech. Rep. June 1994, NASA, Hampton, 1994.

[12] Conlisk, A. T., “Modern helicopter aerodynamics,” *Annual Review of Fluid Mechanics*, Vol. 29, 1997, pp. 515–567. https://doi.org/10.1146/annurev.fluid.29.1.515.

[13] Leishman, J. G., *Principles of Helicopter Aerodynamics*, 2nd ed., Camebridge University Press, 2006.

[14] Raghav, V., Shenoy, R., Smith, M., and Komerath, N., “Investigation of drag and wake turbulence of a rotor hub,” *Aerospace Science and Technology*, Vol. 28, No. 1, 2013, pp. 164–175. https://doi.org/10.1016/j.ast.2012.10.012, URL http://dx.doi.org/10.1016/j.ast.2012.10.012.

[15] Batrakov, A., Garipova, L., Kusyumov, A., Mikhailov, S., and Barakos, G., “Computational fluid dynamics modeling of helicopter fuselage drag,” *Journal of Aircraft*, Vol. 52, No. 5, 2015, pp. 1634–1643. https://doi.org/10.2514/1.C033019.

[16] Raffel, M., Bauknecht, A., Ramasamy, M., Yamauchi, G. K., Heineck, J. T., and Jenkins, L. N., “Contributions of particle image velocimetry to helicopter aerodynamics,” *AIAA Journal*, Vol. 55, No. 9, 2017, pp. 2859–2874. https://doi.org/10.2514/1.J055571.

[17] Seddon, J. M., and Newman, S., *Basic helicopter aerodynamics*, John WIley & Sons, 2011.

[18] Ravi, S., Watkins, S., Watmuff, J., Massey, K., Petersen, P., and Marino, M., “Influence of large-scale freestream turbulence on the performance of a thin airfoil,” *AIAA Journal*, Vol. 50, No. 11, 2012, pp. 2448–2459. https://doi.org/10.2514/1.J051640.

[19] Mücke, T., Kleinhans, D., and Peinke, J., “Atmospheric turbulence and its influence on the alternating loads on wind turbines,” *Wind Energy*, Vol. 14, No. August 2010, 2011, pp. 301–316. https://doi.org/10.1002/we.

[20] Bearman, P. W., and Morel, T., “Effect of free stream turbulence on the flow around bluff bodies,” *Progress in Aerospace Sciences*, Vol. 20, No. 2-3, 1983, pp. 97–123. https://doi.org/10.1016/0376-0421(83)90002-7.

[21] Moradian, N., Ting, D. S., and Cheng, S., “The effects of freestream turbulence on the drag coefficient of a sphere,” *Experimental Thermal and Fluid Science*, Vol. 33, No. 3, 2009, pp. 460–471. https://doi.org/10.1016/j.expthermflusci.2008.11.001, URL http://dx.doi.org/10.1016/j.expthermflusci.2008.11.001.

[22] Trianni, V., and López-Ibánez, M., “Advantages of multi-objective optimisation in evolutionary robotics: survey and case studies,” , No. November, 2014, pp. 1–7. URL http://iridia.ulb.ac.be/IridiaTrSeries/rev/IridiaTr2014-014r002.pdf.

[23] Papoutsis-Kiachagias, E. M., and Giannakoglou, K. C., “Continuous Adjoint Methods for Turbulent Flows, Applied to Shape and Topology Optimization: Industrial Applications,” *Archives of Computational Methods in Engineering*, Vol. 23, No. 2, 2016, pp. 255–299. https://doi.org/10.1007/s11831-014-9141-9, URL http://dx.doi.org/10.1007/s11831-014-9141-9.

[24] Whitley, D., “A genetic algorithm tutorial,” *Statistics and Computing*, Vol. 4, No. 2, 1994, pp. 65–85. https://doi.org/10.1007/BF00175354.

[25] Diez, M., Campana, E. F., and Stern, F., “Stochastic optimization methods for ship resistance and operational efficiency via CFD,” *Structural and Multidisciplinary Optimization*, Vol. 57, No. 2, 2018, pp. 735–758. https://doi.org/10.1007/s00158-017-1775-4.

[26] Jameson, A., and Ou, K., “Optimization Methods in Computational Fluid Dynamics,” *Encyclopedia of Aerospace Engineering*, 2010, pp. 1–14. https://doi.org/10.1002/9780470686652.eae059.

[27] Sefri Hardiansyah, E., “adjointOptimisationFoam, an OpenFOAM-based optimisation tool,” Tech. Rep. 9, National Technical University ofAthens, Athens, 2018.

[28] Pope, S. B., *Turbulent Flows*, 3rd ed., Camebridge University Press, 2000.

[29] Spalart, P., and Allmaras, S., “A one-equation turbulence model for aerodynamic flows,” *30th aerospace sciences meeting and exhibit*, 1992, p. 439. https://doi.org/https://doi.org/10.2514/6.1992-439.

[30] Weller, H. G., Tabor, G., Jasak, H., and Fureby, C., “A tensorial approach to computational continuum mechanics using object-oriented techniques,” *Computers in Physics*, Vol. 12, No. 6, 1998, p. 620. https://doi.org/10.1063/1.168744.

[31] Doormaal, J. P. V., and Raithby, G. D., “ENHANCEMENTS OF THE SIMPLE METHOD FOR PREDICTING INCOMPRESSIBLE FLUID FLOWS,” *Numerical Heat Transfer*, Vol. 7, No. 2, 1984, pp. 147–163. https://doi.org/10.1080/01495728408961817, URL https://doi.org/10.1080/01495728408961817.

[32] Versteeg, H. K., and Malalasekera, W., *An Introduction to Computational Fluid Dynamics - The Finite Volume Method*, 2^{nd} ed., Pearson Education Limited, Essex, 2007.

[33] Anderson, J. D., and Wendt, J., *Computational fluid dynamics*, 3^{rd} ed., Springer, 1995.

[34] Saad, Y., *Iterative methods for sparse linear systems*, SIAM, 2000.

[35] Gisen, D., “Generation of a 3D Mesh Using snappyHexMesh Featuring Anisotropic Refinement and Near-wall Layers,” *ICHE 2014. Proceedings of the 11th International Conference on Hydroscience & Engineering*, 2014, pp. 983–990. URL https://henry.baw.de/handle/20.500.11970/99527?locale-attribute=en.

[36] NASA, “The Spalart-Allmaras Turbulence Model,” , 2020. URL https://turbmodels.larc.nasa.gov/spalart.html.

[37] Celik, I. B., Ghia, U., Roache, P. J., Freitas, C. J., Coleman, H., and Raad, P. E., “Procedure for estimation and reporting of uncertainty due to discretization in CFD applications,” *Journal of Fluids Engineering, Transactions of the ASME*, Vol. 130, No. 7, 2008, pp. 0780011–0780014. https://doi.org/10.1115/1.2960953.

[38] Yu, D., and Kareem, A., “Parametric study of flow around rectangular prisms using LES,” *Journal of Wind Engineering and Industrial Aerodynamics*, Vol. 77-78, 1998, pp. 653–662. https://doi.org/10.1016/S0167-6105(98)00180-9.

[39] Spalart, P. R., and Garbaruk, A. V., “Correction to the Spalart-Allmaras turbulence model, providing more accurate skin friction,” *AIAA Journal*, Vol. 58, No. 5, 2020, pp. 1903–1905. https://doi.org/10.2514/1.J059489.

[40] Winslow, J., Otsuka, H., Govindarajan, B., and Chopra, I., “Basic understanding of airfoil characteristics at low Reynolds numbers (104–105),” *Journal of Aircraft*, Vol. 55, No. 3, 2018, pp. 1050–1061. https://doi.org/10.2514/1.C034415.

A. Numerical simulations

A. Turbulence model

For the problem at hand we use the steady Reynolds averaged Navier-Stokes equations, given in Eqs. (A-1),(A-2).

$$\int_A \overline{\mathbf{u}} \cdot \mathbf{n} dA = 0, \tag{A-1}$$

$$\frac{\partial}{\partial t}\int_V \overline{\mathbf{u}} dV + \int_A \overline{\mathbf{u}}\ (\overline{\mathbf{u}} \cdot \mathbf{n})\, dA = -\frac{1}{\rho}\int_A \overline{p} \cdot \mathbf{n} dA + \int_A \nu(\nabla\overline{\mathbf{u}}) \cdot \mathbf{n} dA - \int_A \overline{\mathbf{u}'\mathbf{u}'} \cdot \mathbf{n} dA. \tag{A-2}$$

$\overline{\mathbf{u}}$ denotes the average velocity and $\mathbf{u}^{'}$ the velocity fluctuation. The Reynolds stress term, the last term on the right hand side in Eq. A-2, is approximated through the Boussinesq hypothesis [28] which relates the term to the mean flow quantities and reads

$$-\left(\overline{\mathbf{u}'\mathbf{u}'}\right) = \nu_T \left(\frac{\partial u_i}{\partial x_j} + \frac{\partial u_j}{\partial x_i}\right) \tag{A-3}$$

when the Spalart-Allmaras turbulence model is applied. δ_{ij} denotes the Kronecker-delta, the term ν_T is the turbulent viscosity and is modelled through the use of a turbulence model. The turbulent viscosity is modelled with the spalart-Allmaras [29] turbulence model. In OpenFOAM® the Spalart-Allmaras model is implemented as

$$\frac{\partial\tilde{\nu}}{\partial t} + \overline{\mathbf{u}} \cdot \nabla\tilde{\nu} = C_{b1}\tilde{S}\tilde{\nu} - C_{w1} f_w \left(\frac{\tilde{\nu}}{d}\right)^2 + \frac{1}{\sigma_{\nu_T}}\left[\nabla \cdot \left((\nu + \tilde{\nu})\nabla\right) + C_{b2}\left(\nabla\tilde{\nu}\right)^2\right] \tag{A-4}$$

where

$$f_{v1} = \frac{\chi^3}{\chi^3 + C_{v1}^3}, \qquad \chi = \frac{\tilde{\nu}}{\nu}, \qquad \tilde{S} = S^{\frac{1}{2}} + \frac{\tilde{\nu}}{\kappa d^2} f_{v2} \tag{A-5}$$

$$f_{v2} = 1 - \frac{\chi}{1 + \chi f_{v1}}, \qquad f_w = g\left(\frac{1 + c_{w3}^6}{g^6 + c_{w3}^6}\right)^{\frac{1}{6}}, \qquad g = r + c_{w2}\left(r^6 - r\right) \tag{A-6}$$

$$r = \frac{\tilde{\nu}}{\tilde{S}\kappa^2 d^2}, \qquad c_{w1} = \frac{c_{b1}}{\kappa} + \frac{1 + c_{b2}}{\sigma_{\nu_T}} \tag{A-7}$$

d is the distance from the wall and the constants are listed in table A-1.

Table A-1 Default coefficients used in the Spalart-Allmaras turbulence model in OpenFOAM®.

σ_{ν_T}	C_{b1}	C_{b2}	C_{w2}	C_{w3}	C_{ν_T}	κ
$\frac{2}{3}$	0.1355	0.622	0.3	2	7.1	0.41

Finally the turbulent eddy viscosity is given as

$$\nu_T = f_{v1}\tilde{\nu}. \tag{A-8}$$

B. Grid Convergence method

A method to evaluate the discretization error in CFD simulations was developed by [37] using Richardison extrapolation and will be reported here. Before the discretization error is estimated we must show that iterative convergence has been reached. This is done by showing that the normalized residuals are converged by at least three order of magnitudes and that a monitored variable has stabilized. Defining a representative cell h as

$$h = \left[\frac{1}{N}\sum_{i=1}^{N}(\Delta V_i)\right]^{\frac{1}{3}} \tag{A-9}$$

where ΔV_i is the ith cell volume and N the number of cells of the mesh. We use three significantly different grids, yet refined in a structured way and calculate the value of h for each one. Define

$$r_{21} = \frac{h_2}{h_1}, \tag{A-10}$$

$$r_{32} = \frac{h_3}{h_2}, \tag{A-11}$$

where 3 is the coarsest mesh and 1 the finest mesh. We choose a meaningful variable ϕ, e.g the drag coefficient C_D, that must be solved for all the meshes and then compared. For example, we can calculate the difference between the different estimates of the values such as

$$\epsilon_{21} = \phi_2 - \phi_1, \tag{A-12}$$

$$\epsilon_{32} = \phi_3 - \phi_2. \tag{A-13}$$

Ideally, the convergence of the monitored variable should be non-oscillatory. The apparent order p of the simulation can then be calculated by

$$p = \frac{1}{ln(r_{21})} \left| \frac{\epsilon_{32}}{\epsilon_{21}} + q(p) \right| \tag{A-14}$$

where $q(p)$ is given by

$$q(p) = ln \left(\frac{r_{21}^p - s}{r_{32}^p - s} \right), \tag{A-15}$$

and s is

$$s = sgn(\frac{\epsilon_{32}}{\epsilon_{21}}). \tag{A-16}$$

This set of equations can be solved through fixed point iteration. Finally, the extrapolated error can be calculated as

$$\phi_{ext}^{21} = \frac{(r_{21}^p \phi_1 - \phi_2)}{r_{21}^p - 1}, \tag{A-17}$$

and

$$\phi_{ext}^{32} = \frac{(r_{32}^p \phi_1 - \phi_2)}{r_{32}^p - 1}. \tag{A-18}$$

The approximative relative error is then given by

$$e_a^{21} = \left| \frac{\phi_1 - \phi_2}{\phi_1} \right|, \tag{A-19}$$

the extrapolated relative error as

$$e_{ext}^{21} = \left| \frac{\phi_{ext}^{12} - \phi_1}{\phi_{ext}^{12}} \right|, \tag{A-20}$$

and finally the GCI as

$$GCI_{fine}^{21} = \frac{1.25 e_a^{21}}{r_{21}^p - 1}. \tag{A-21}$$

B. Wind tunnel refurbishment

As a part of the thesis I contributed to the refurbishing of the large closed loop wind tunnel at NTNU. Hereby I include some images with a short description of the work done, see Fig. B.1a, B.1b, B.2a, B.2b, B.3a, B.3b, B.4a and B.4b. In Fig. B.5 the newly refurbished test-section and parts of the wind tunnel is shown. The work shown here was done in a collaborative manner with several students, PhD-candidates and staff from NTNU, and not independently by me.

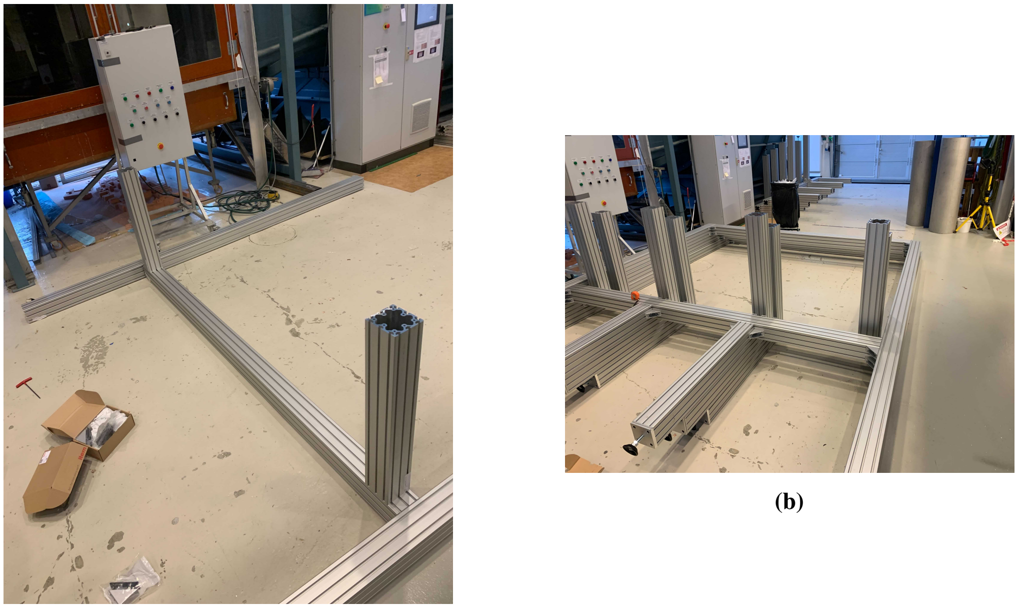

(a)

(b)

Fig. B.1 Mounting of the frames for the new wind tunnel test section. The aluflex pieces were mounted with angle brackets.

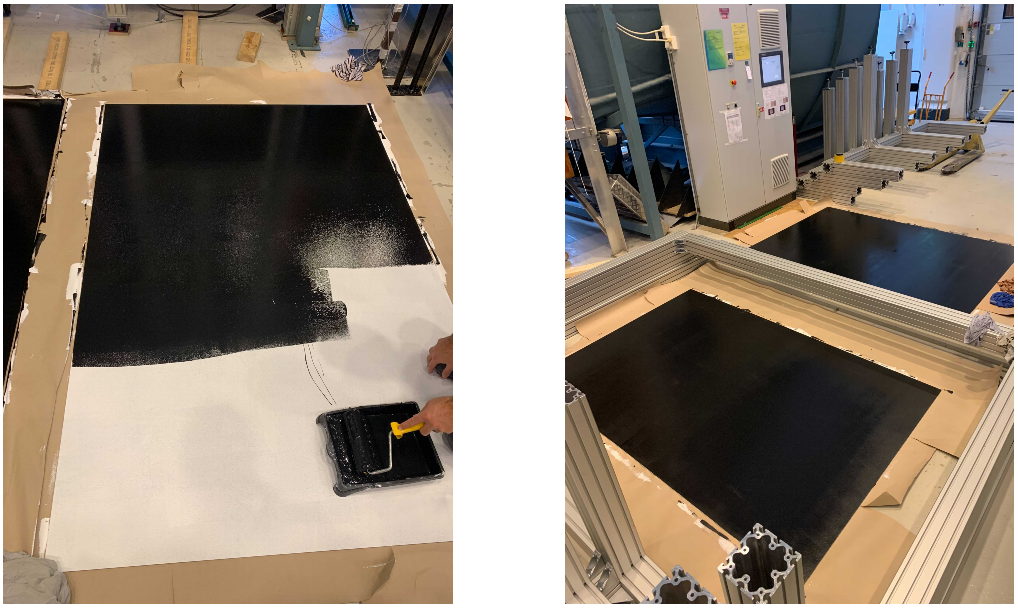

(a)

(b)

Fig. B.2 Sanded and painted steel plates used as walls in the new test section of the wind tunnel.

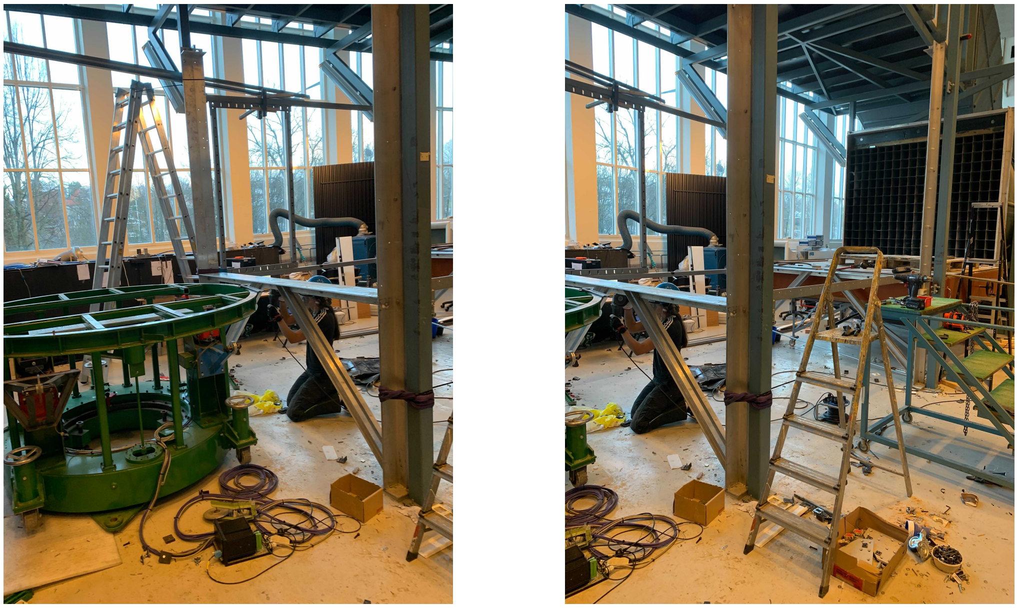

(a) (b)

Fig. B.3 To install the new test section we dismantled the old test section. Removing large steel beams safely in a confined space required some creativity.

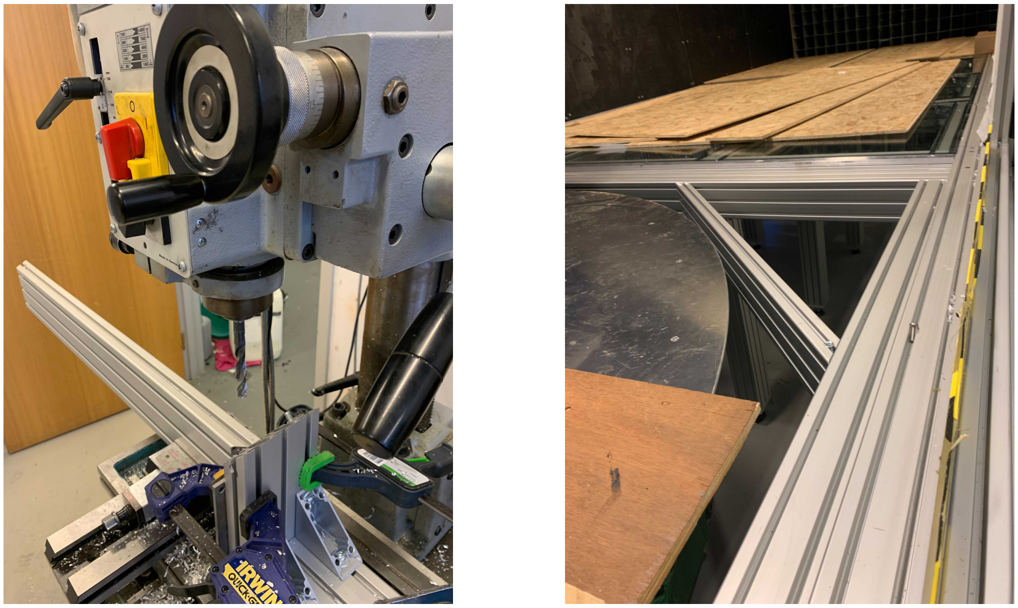

(a) (b)

Fig. B.4 Measured, cut, drilled and mounted a support structure for the floor around the load balance. With help from Olav Rømcke I learned to use the drill press and the aluminum saw.

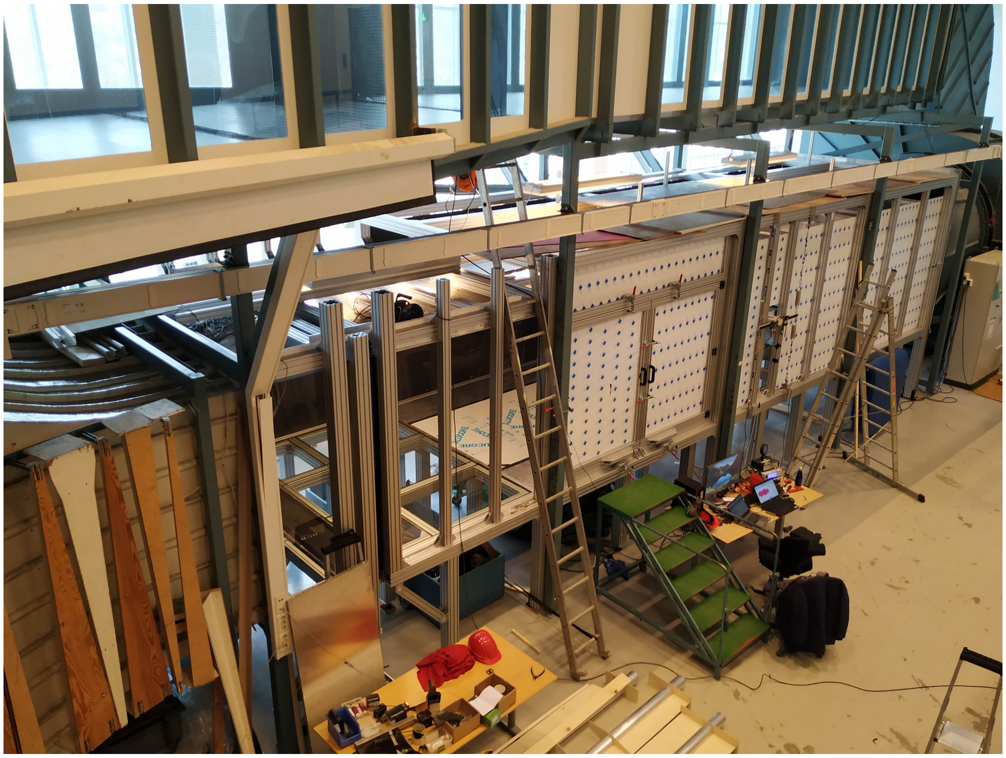

Fig. B.5 The newly refurbished wind tunnel test-section. Image courtesy of Magnus Kyrkjebø Vinnes.

NTNU

Norwegian University of
Science and Technology